



Hybrid phase-field modeling of multi-level concrete gravity dam notched cracks

H. Mazighi, M.K. Mihoubi

Mobilisation et Valorisation des Ressources en Eau (MVRE), Ecole Nationale Supérieure d'Hydraulique (ENSH), Blida, Algeria.

h.mazighi@ensh.dz, https://orcid.org/0000-0001-5983-5473

mihkam@ensh.dz, https://orcid.org/0000-0002-7858-0127

D. Santillán

Dept. de Ingeniería Civil: Hidráulica, Energía y Medio Ambiente, Universidad Politécnica de Madrid, Madrid, 28040, Spain
david.santillan@upm.es, https://orcid.org/0000-0002-9749-0522

ABSTRACT. Phase-field models have become a powerful tool to simulate crack propagation. They regularize the fracture discontinuity and smooth the transition between the intact and the damaged regions. Based on the thermodynamic function and a diffusive field, they regularize the variational approach to fracture that generalizes Griffith's theory for brittle fracture. Phase-field models are capable to simulate complex fracture patterns efficiently and straightforwardly. In this paper, we introduce a hybrid phase-field approach to simulate the crack propagation in laboratory-scale and life-scale structures. First, we apply our methodology to the three-point bending test on notched laboratory beams. Second, we simulate the fracture propagation in a life-size structure: the Koyna gravity dam. We account for the pressure load inside the fracture, and we study the effect of the position and number of initial fractures in the upstream face and the value of the Griffith critical energy release, on the fracture propagation under a flood event. The position of the fracture plays an important role in the final fracture pattern and crest displacements, whereas the value of the Griffith critical energy release alters the onset of the fracture propagation. We conclude that phase-field models are a promising computational tool that may be applied to real engineering problems.

OPEN ACCESS

Citation: Mazighi, H., Mihoubi, M.K., Santillán, D., Hybrid phase-field modeling of multi-level concrete gravity dam notches crack, *Frattura ed Integrità Strutturale*, 61 (2022) 154-175.

Received: 24.01.2022

Accepted: 21.03.2022

Online first: 30.04.2022

Published: 01.07.2022

Copyright: © 2022 This is an open access article under the terms of the CC-BY 4.0, which permits unrestricted use, distribution, and reproduction in any medium, provided the original author and source are credited.

KEYWORDS. Concrete; Crack; Dam; Fluid pressure; Phase-field model.



INTRODUCTION

Concrete is one of the most common building materials in the world, and society demands proper safety levels in those infrastructures made of concrete. Safety assessment tasks require predicting the behavior of the structures until their ruin [1,2]. Engineers demand numerical models to simulate the fracture process. In this line, the two most employed approaches aiming at the initiation, localization, and propagation of cracks are the continuous [3] and discontinuous models [4].

The fracture is considered a discontinuity in the material due to internal or external stresses. The two most widely used theories in fracture mechanics are the Linear Elastic Fracture Mechanics (LEFM) [1,5] and Nonlinear Fracture Mechanics (NLFM) [6–9]. The latter theory adopts the nonlinear behaviors which take into account micro-cracks located near the crack tip, the so-called fracture process zone [10]. This theory is suitable for large structures i.e. dams, bridges, etc. Contrary to the NLFM, the LEFM approach is simpler and assumes linear elastic behavior of materials [11].

In parallel, Continuum Damage Mechanics (CDM) [12,13] is a robust concept to model the degradation of materials, leading to the localization of fractures [14,15]. Many models have been proposed to simulate damage in concrete based on CDM [16–25]. Significant research efforts on modeling cracks have been conducted using the Finite Element Method (FEM) [26–34], and the Extended Finite Element Method (XFEM) [35–43].

Recently, a new continuous model has appeared acknowledged as phase-field [44–47]. It models the discontinuities as a diffusive process and interpolates between both the broken and unbroken regions, the crack is determined by a scalar variable that takes two distinct values (0 inside the crack and 1 away) [48,49]. The damaged regions are determined by a coupled system of Partial Differential Equations (PDEs) based on the energy minimization; thus, additional computations as stress intensity factors are not necessary to calculate the crack initiation and propagation [50]. However, the method requires a regularization parameter called length scale [51], recently validated with experiments [52]. The great advantage of the phase-field approach is the ability to simulate complex crack patterns, such as twisting, kriging, joining [53,54]. It provides excellent results for brittle fracture [49,54–57], ductile fracture [58–61], cohesive fracture [62–64], and other complex applications [50].

In this paper, we focus on the ability of phase-field models to simulate the propagation of multi-level notched cracks in large structures, such as dams, and study its influence on the behavior of the structure compared to the load exerted by the fluid pressure inside the fracture. A recent and robust hybrid formulation of continuum damage mechanics is adopted to solve the governing PDEs due to its low computational cost. Our model encompasses all results previously found by other researchers considering the most influential basic parameters and possible crack levels.

The paper is organized as follows: first, we present the governing equation of our model; afterward, we validate our model by comparing our numerical results with reported laboratory experiments on the literature; thereafter, we simulate the fracture propagation in a live-size gravity dam. Finally, we draw some overall conclusions.

GOVERNING EQUATIONS

This section introduces the coupled mathematical equations for fracture propagation in quasi-brittle materials. Once presented with the geometry of the domain, we derive the PDEs that govern our problem.

Geometry

Fig. 1 shows the proposed geometry, where the domain $\Omega \subset \mathbb{R}^3$ has dimension $\delta \in \{1,2,3\}$. Ω is composed of two subdomains, the elastic Ω_E , and the fracture Ω_F . The boundary conditions applied on the subdomain Ω_E can be time-dependent Dirichlet conditions on $\partial_D \Omega_E$ or time-dependent Neumann conditions on $\partial_N \Omega_E$. We denote with $f(x,t)$ the external traction force applied on $\partial_N \Omega_E$, $b(x,t)$ is the body force, x is the position vector, and $u(x,t) \subset \mathbb{R}^3$ is the displacement field at time t .

Constitutive relations

We compute the crack propagation in quasi-brittle material through a quasi-static phase-field formulation, based on Griffith's theory, an energy-based failure criterion propagation in brittle materials [1]. The crack propagates when the stored energy is higher than the fracture resistance of the material.

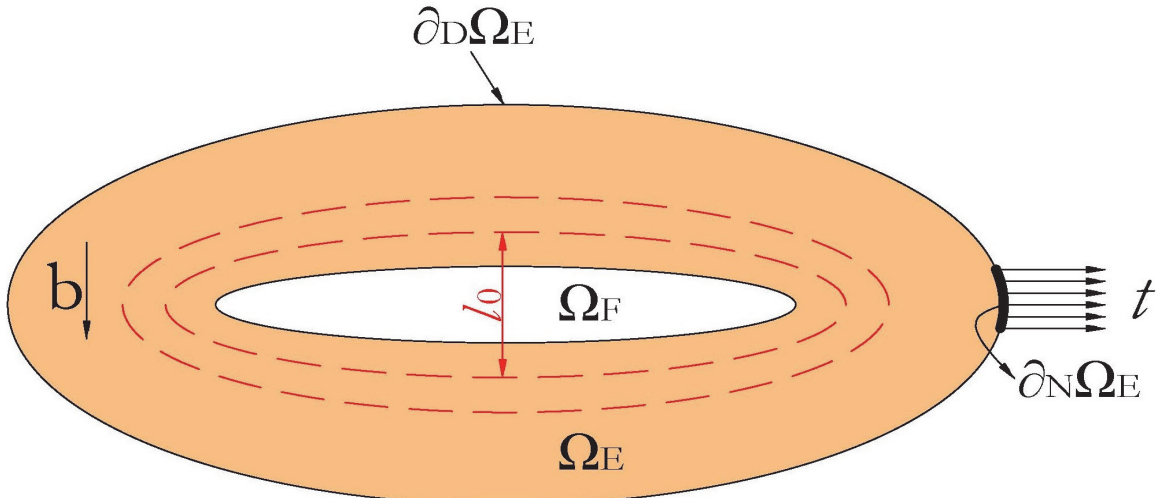


Figure 1: Scheme of the domains of the problem.

The crack propagation states the minimization of the total potential energy stored ψ :

$$\psi = \psi^d + \psi^e - \psi^s \quad (1)$$

where ψ^d is the critical energy release during the fracture process, ψ^e is the elastic energy, and ψ^s are the external sources of energy due to body and surface loads. The critical energy release during the fracture propagation equals:

$$\psi^d = \int_{\partial\Omega_F} G_c dS = \int_{\Omega_F} G_c \gamma_l d\Omega \quad (2)$$

where G_c is the Griffith critical energy release rate for mode-I of fracture, and γ_l is the crack surface density per unit volume of the solid, given by Miehe et al. [48]:

$$\gamma_l(\phi, \nabla\phi) = \frac{\phi^2}{2l_0} + \frac{l_0}{2} |\nabla\phi|^2 \quad (3)$$

where l_0 is the length scale parameter, and ϕ is the phase-field which satisfies the following condition:

$$\phi(x,t) = \begin{cases} 0, & \text{if the material is intact} \\ 1, & \text{if the material is cracked} \end{cases} \quad (4)$$

Therefore, ψ^d equals:

$$\psi^d = \int_{\Omega_F} G_c \left(\frac{\phi^2}{2l_0} + \frac{l_0}{2} |\nabla\phi|^2 \right) d\Omega \quad (5)$$

Borden et al. and Zhang et al. [65,66] proposed an analytical solution for computing the length scale parameter, l_0 , which depends on the resistance tensile strength, f_t , the Young's Modulus, E , and the Griffith critical energy release rate, G_c , as follows:

$$l_0 = \frac{27EG_c}{256f_t^2} \quad (6)$$

In Eqn. (5), the critical energy release can be calculated through [67]:

$$G_c = \begin{cases} \frac{K_{lc}^2}{E} (1-\nu^2), & \text{plane strain} \\ \frac{K_{lc}^2}{E}, & \text{plane stress} \end{cases} \quad (7)$$

where K_{lc} is the fracture toughness and ν is the Poisson's ratio.

The strain tensor is decomposed into two parts [68]:

$$\varepsilon_{\pm} = \sum_{a=1}^{\delta} \varepsilon_{a\pm} n_a \otimes n_a \quad (8)$$

where ε_+ and ε_- are the tensile and compressive strain tensors, respectively, ε_a is the a^{th} principal strain, and n_a is the principal direction of strain tensor ε_a . The elastic energies are expressed as:

$$\psi_e^{\pm}(\varepsilon) = \frac{\lambda}{2} \text{tr}(\varepsilon_{\pm}^2) + \mu \text{tr}(\varepsilon_{\pm}^2) \quad (9)$$

where λ and μ are Lamé constants, given by:

$$\begin{cases} \lambda = \frac{\nu E}{(1+\nu)(1-2\nu)}, \quad \mu = \frac{E}{2(1+\nu)} & \text{plane strain} \\ \lambda = \frac{\nu E}{(1+\nu)(1-\nu)}, \quad \mu = \frac{E(1+2\nu)}{3(1+\nu)(1-\nu)} & \text{plane stress} \end{cases} \quad (10)$$

The strain tensor is related to the displacement field u by:

$$\varepsilon = \frac{1}{2} (\nabla u + \nabla u^T) \quad (11)$$

We adopt the anisotropic formulation proposed by Miehe et al. [68], which states that fractures only propagate under tension, i.e., due to the positive part of the elastic energy. The total elastic energy is then expressed as:

$$\psi_e^{\pm}(\varepsilon) = g(\phi) \psi_e^+(\varepsilon) + \psi_e^-(\varepsilon) \quad (12)$$

where $g(\phi) = (1-k)(1-\phi^2) + k$ is the degradation function, and k ($0 < k \ll 1$) is a parameter that avoids numerical singularities.

The external energy functional, ψ^s accounts for the body forces and the applied loads on the boundaries as follows:

$$\psi^s = \int_{\Omega} \bar{f} \cdot u \, d\Omega + \int_{\partial\Omega_E} \bar{t} \cdot u \, d\partial \quad (13)$$

The fluid pressure inside the fracture, p_f , exerts a force on the surface of the fracture. We include this load in the term of traction vector force as follows:

$$\int_{\partial\Omega_E} \bar{t} \cdot u \, d\partial = \int_{\partial_N \Omega} \bar{t} \cdot u \, d\partial - \int_{\partial_N \Omega_F} p_f \bar{n} \cdot u \, d\partial \quad (14)$$

We develop the second term in Eqn. (14) using the Divergence Theorem as follows:



$$\int_{\partial_N \Omega_F} p_f \bar{n} \cdot u \, d\partial = \int_{\Omega_E} \nabla \cdot (p_f u) \, d\Omega - \int_{\partial_N \Omega_E} p_f \bar{n} \cdot u \, d\partial \quad (15)$$

The pressure load on the surface of the fracture is then formulated as a body force applied to the entire domain. To consider the crack propagation, we introduce the phase-field in Eqn. (15):

$$\int_{\Omega_E} \nabla \cdot (p_f u) \, d\Omega - \int_{\partial_N \Omega_E} p_f \bar{n} \cdot u \, d\partial = \int_{\Omega} g(\phi) \nabla \cdot (p_f u) \, d\Omega - \int_{\partial_N \Omega} g(\phi) p_f \bar{n} \cdot u \, d\partial \quad (16)$$

Thus, the external energy ψ^S becomes:

$$\psi^S = \int_{\Omega} \bar{f} \cdot u \, d\Omega - \int_{\Omega} g(\phi) \nabla \cdot (p_f u) \, d\Omega + \int_{\partial_N \Omega} g(\phi) p_f \bar{n} \cdot u \, d\partial + \int_{\partial_N \Omega} \bar{t} \cdot u \, d\partial \quad (17)$$

By substituting Eqns. (5), (12), and (17) into Eqn. (1), the Fréchet derivative of the total potential energy ψ yields the following Euler equations [65]:

$$\frac{G_c}{l_0} (\phi - l_0^2 \nabla^2 \phi) = 2(1-k)(1-\phi) [\psi_e^+(\epsilon) + p_f \nabla \cdot u + u \cdot \nabla p_f] \quad (18)$$

and:

$$\nabla \sigma + p_f \nabla g(\phi) + \bar{f} = 0 \quad (19)$$

where the Cauchy stress tensor is given by:

$$\sigma = g(\phi) [\lambda \text{tr}(\epsilon)_+ I + 2\mu \epsilon_+] + \lambda \text{tr}(\epsilon)_- I + 2\mu \quad (20)$$

The regime flow inside the porous media material is based on Darcy's law, which is derived from the Navier-Stokes equation. It describes a linear relationship between the velocity v (m/s) and the gradient of pressure p_f (Pa). Lomiz [69] and Louis [70] carried out that the penetration of the fluid through a rock fracture follows the Cubic law developed using the parallel-plates approach [71].

$$\nabla p_f = \frac{\mu}{k} v \quad (21)$$

with μ the dynamic viscosity (Pa.s) and k (m^2) the permeability of the porous medium of the fluid respectively.

Darcy's law is only valid for low velocities when the regime is laminar [69,70].

We account for the irreversibility of the crack propagation process by adopting the following strain-history field $H^+(u, p_f, t)$ [72]:

$$H^+(u, p_f, t) = \max_{x \in [0, t]} (\psi_e^+(\epsilon) + p_f \nabla \cdot u + u \cdot \nabla p_f) \quad (22)$$

Eqn. (18) can then be rewritten as:

$$\frac{G_c}{l_0} (\phi - l_0^2 \nabla^2 \phi) = 2(1-k)(1-\phi) H^+ \quad (23)$$

Thereby, the Euler-Lagrangian equation becomes:



$$\begin{cases} \nabla\sigma + p_f \nabla g(\phi) + \bar{f} = 0 \\ \left[\frac{2l_0(1-k)H^+}{G_c} + 1 \right] \phi - l_0^2 \nabla^2 \phi = \frac{2l_0(1-k)H^+}{G_c} \end{cases} \quad (24)$$

Eqn. (24) are the strong form of the phase-field problem, subject to the following Neumann boundary conditions:

$$\begin{cases} \sigma \cdot \bar{n} = \bar{t} + g(d)p_f & \text{in } \partial_N \Omega \\ \nabla \phi \cdot \bar{n} = 0 & \text{in } \partial_N \Omega \end{cases} \quad (25)$$

Eqn. (24) summarizes the nonlinear phase-field problem. The equations include the decomposition of the Cauchy stress tensor into its compression and tension parts. Since we assume fractures only propagate under tension, and not due to compression, the degradation function only affects the positive elastic energy. From a mathematical point of view, this assumption leads to a highly nonlinear and computationally expensive system of PDEs. Recently, these drawbacks have been sorted out with the so-called hybrid formulation [73]. The formulation linearizes the problem with a third constraint as follows:

$$\begin{cases} \nabla\sigma + p_f \nabla g(\phi) + \bar{f} = 0 \\ \left[\frac{2l_0(1-k)H^+}{G_c} + 1 \right] \phi - l_0^2 \nabla^2 \phi = \frac{2l_0(1-k)H^+}{G_c} \\ \forall x: \psi_e^+ < \psi_e^- \Rightarrow \phi := 0 \end{cases} \quad (26)$$

In quasi-static calculation, the fractures propagate under a toughness-dominated regime. The energy expended during the fracture process is much higher than the viscous dissipation [74], i.e., the energy dissipated due to the water flow within the fracture. This assumption involves that the water pressure inside the crack is more or less constant and equal to the hydrostatic pressure at the crack level [50]. Consequently, the term $u \cdot \nabla p_f$ in Eqn. (22) is null.

We solve the system of PDEs given by Eqn. (26) with the staggered scheme proposed by Miehe et al. [72], successfully used in engineering problems [50,75]. The displacement field, u , the phase-field, ϕ , and the strain-history field, H^+ , are solved sequentially, as shown in Fig. 2. This approach requires small loading increments, i.e., small-time steps [50]. We adopt an implicit Backward Differentiation Formula [76] for the time integration. At the beginning of the $j+1$ time step, we take as the initial condition, the solution of the previous time step, j . The displacement field is first computed using H^{+j} and ϕ^j . Afterward, the stain-history field is updated with u^{j+1} and ϕ^j . Finally, the phase-field is updated. In each time step, a minimum tolerance convergence is required.

MODEL VALIDATION

The purpose of the study proposed in this section is to validate the numerical model presented previously. The validation consists to compare the obtained results from the application of our numerical model on a benchmark widely used in fracture mechanics, which is the notched beam problem, where experimental data are available.

Notched concrete beam

In this example, we simulate the propagation of a fracture in the notched beam problem [77]. The geometry is depicted in Fig. 3(a), according to Meschke et al. [78]. The thickness of the beam is 127 mm, the height is 254 mm, the length is 1118 mm, and the span is 1016 mm. The mechanical properties are: $E = 4.36 \times 10^4$ MPa, $\nu = 0.2$, $f_t = 4.0$ MPa, and $G_c = 119$ N/m. We simulate the propagation of an initial vertical fracture parallel to the side of the beam. The fracture is 78 mm in length and 5 mm in width and is located in the bottom part of the beam. We apply an incremental vertical displacement u on the top central part of the beam, and we neglect the self-weight. We adopt as length scale parameter $l_0 = 10$ mm.

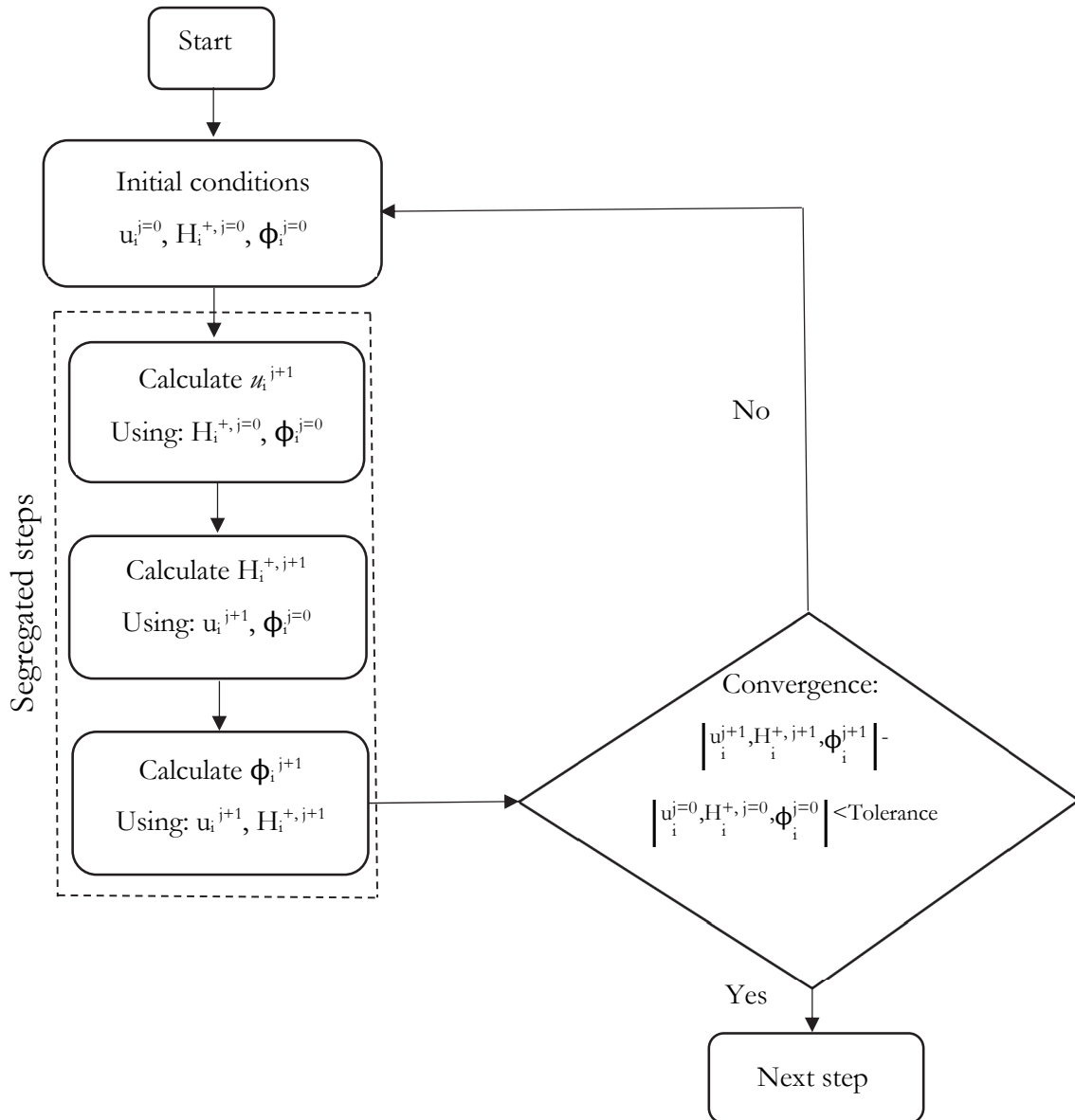


Figure 2: Staged scheme for the numerical resolution of the PDE system.

We simulate the fracture propagation with a 2-dimensional model under plane strain conditions. We discretize the domain around the fracture with 8272 quadrilateral elements and the rest of the beam with 6427 triangular elements. The mesh size around the fracture is $h_0 = 1.0 \text{ mm} = l_0/10$, small enough to accurately capture the transition from damaged to undamaged regions.

We plot the fracture pattern in Fig. 3(b), where the red color represents the fracture, and the evolution of the applied force against the Crack Mouth Opening Distance (CMOD) in Fig. 3(c). We compare our simulations with those reported by Meschke et al. and Mandal et al. [78,79], and experimental results. Our simulations are quite similar to both reported results as well as with laboratory experiments. The applied load increases linearly until the critical load is reached. Afterward, the crack grows quickly, and the CMOD increases.

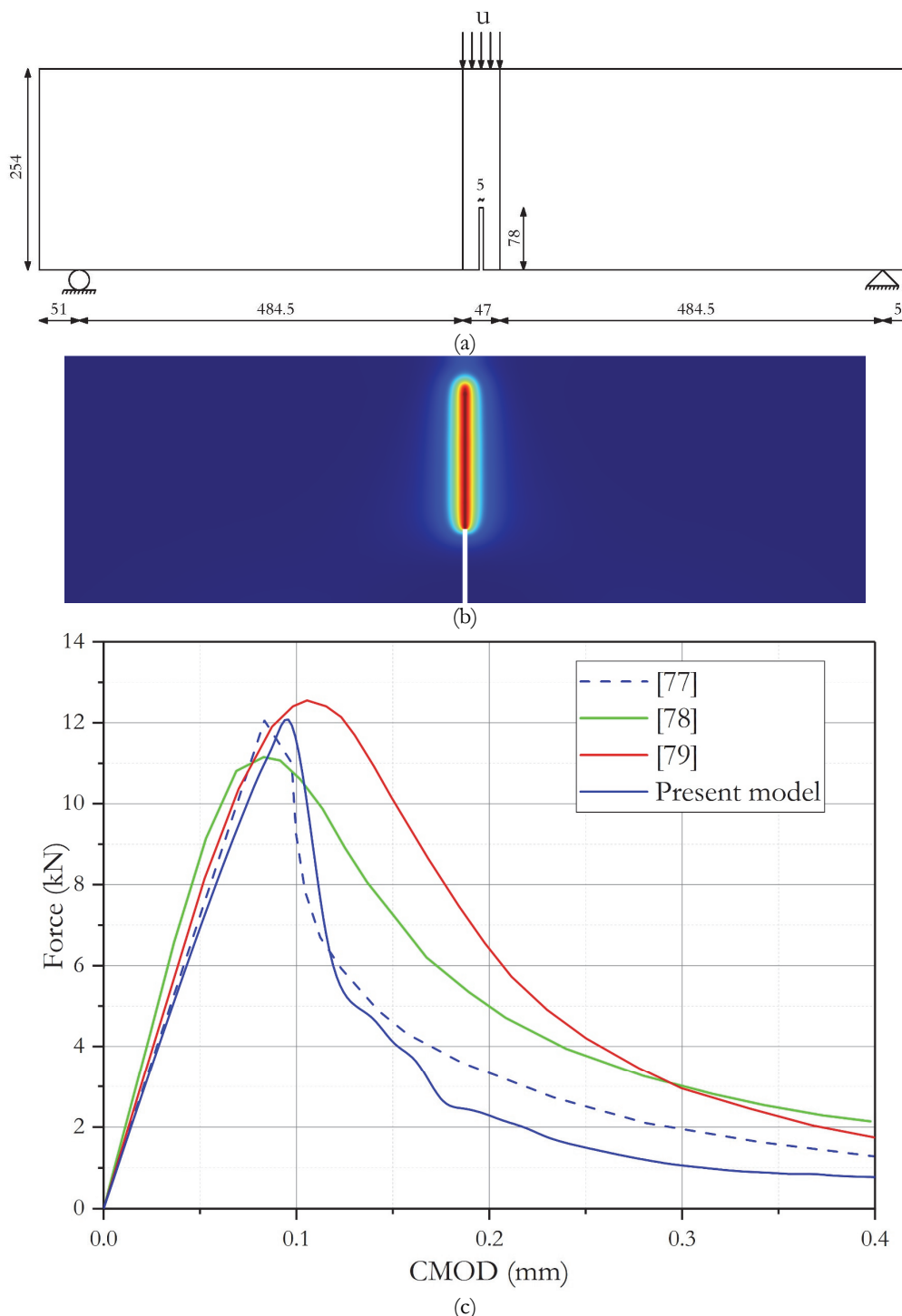


Figure 3: (a) Geometry and boundary conditions of the notched beam test. Dimensions are in mm. (b) Fracture pattern. (c) Evolution of the applied force against CMOD.

FULL-SCALE CONCRETE GRAVITY DAM

Our second benchmark is a life-size structure, the Koyna gravity dam. The propagation of fracture along the dam body has been previously simulated by many researchers. We assume plane-strain conditions and homogenous materials. The structure is 103 m in height and is located in India. It has been widely used as a benchmark model



for static analysis of fracture propagation with 2-dimensional mathematical models. Gioia et al. [80] compared fracture analyses of notched the Koyna dam using plastic and linear elastic fracture mechanics, the effect of three initial horizontal cracks on the upstream face on the failure process of the structure is studied as well. The authors concluded that the most critical position of the initial fracture is at the change of the downstream slope. Bhattacharjee and Léger [81] employed two smeared models based on nonlinear fracture mechanics to study the behavior of the dam under two critical energy dissipation parameters. The results showed that the critical energy affects considerably the initiation of the crack. Ghrib and Tinawi [82] proposed an anisotropic continuous damage model formulation and studied the influence of mesh size. The fracture becomes smoother as the mesh is refined, but no major changes in the crest displacement were detected. Roth et al. [83] adopted a coupled anisotropic damage mechanic model based on the continuous approach and XFEM to simulate the fracture propagation in the Koyna dam. The level sets functions used to define the fracture path, together the continuum damage mechanics provided a correct fracture path. Santillán et al. [50] implemented a hybrid-phase field model to simulate the failure of the Koyna dam. The authors disregarded the pressure load inside the fracture, yet they found a good agreement with the results of Bažant, Z.P., Planas [84].

In this study, we adopt our hybrid model and incorporate the effect of the pressure load inside the fracture. We study the influence of the initial crack level, the number, and length of initial fractures, as well as the value of the critical energy dissipation on the behavior of the dam under a flood event. We illustrate the Koyna dam geometry in Fig. 4(a), where we also depict the three initial fracture levels in the upstream face denoted as crack I, crack II, and crack III. The distance between crack levels is 22.17 m which corresponds to one-third of 66.51 m, and the depth of the fractures is $0.1B_i$, where B_i is the width of the dam at the given height.

The applied loads on the dam are the hydrostatic load plus the overflow on the upstream face, and the self-weight. The mechanical properties of the concrete are taken from the simulations of Bhattacharjee and Léger [81], and these are: Young Modulus $E = 25000$ MPa, $\nu = 0.2$, $f_t = 1.0$ MPa, $\rho = 2450$ kg/m³. Regarding the Griffith critical energy release rate, we adopt two plausible values: $G_c = 100$ N/m and $G_c = 200$ N/m, with $l_0 = 0.4$ m. For each value of the critical energy release rate, we analyze the effect of the initial length and location of the crack on the fracture path and the evolution of the horizontal crest displacement. In this line, we have conducted four simulations for each G_c -value:

- Case I. Dam with an initial horizontal fracture on the upstream face at height 66.51 m.
- Case II. Dam with an initial horizontal fracture on the upstream face at height 44.34 m.
- Case III. Dam with an initial horizontal fracture on the upstream face at height 22.17 m
- Case IV: Dam with three initial horizontal fractures on the upstream face at the heights 22.17, 44.34, and 66.51 m respectively.

We simulate the fracture propagation with a 2-dimensional model under plane strain conditions. We discretize the domain around the fracture path with structured quadrilateral elements of 8 cm size and triangular elements in the remaining parts of the dam. We include the fracture paths for Case I and $G_c = 100$ N/m reported in previous works in Fig. 4(b), and the evolution of the overflow against the horizontal displacement of the crest in Fig. 4(c).

Simulation for a rate $G_c=100$ N/m

The evolution of the overflow against the horizontal crest displacement for Case I is depicted in Fig. 5(a). We depict the contour plots of the phase-field at four-time steps, denoted from A to C in the plot of the panel (a). The initial fracture begins to propagate when the overflow is 6.11 m (point A). The crest displacement is linear with the overflow, but once the water level is 6.11 m above the crest, a sudden growth of the fracture occurs. The propagation of the fracture makes the crest displacement increase suddenly while the water level remains constant (transition from time step A to B). The fracture path at time step B is shown in Fig. 5(b).

After the initial sudden fracture growth, the crack propagates slowly. The crest displacement is no longer linear with overflow, indeed the displacement grows with a lower increase of the water level than before. This behavior changes at time step C, where a sudden propagation of the fracture occurs again. Between the time steps B and C the fracture branches, a new sub-vertical fracture appears that heads towards the change of slope in the downstream face. After time step D, both fractures continue the propagation. The crest displacement is then higher for lower rises of the water level.

The results of Case II are included in Fig. 6. The evolution of the crest displacement against the overflow is plotted in panel (a), and the fracture pattern at the last time step of the simulation is shown in panel (b). As in the previous case, initially, the crest displacement is linear with the overflow. The fracture begins to propagate when the water level is about 7 m. Afterward, the fracture grows slowly, but the crest displacement is no longer linear with the water level, and the slope of the curve water level-crest displacement changes. We stop the simulation when the overflow is 11 m.

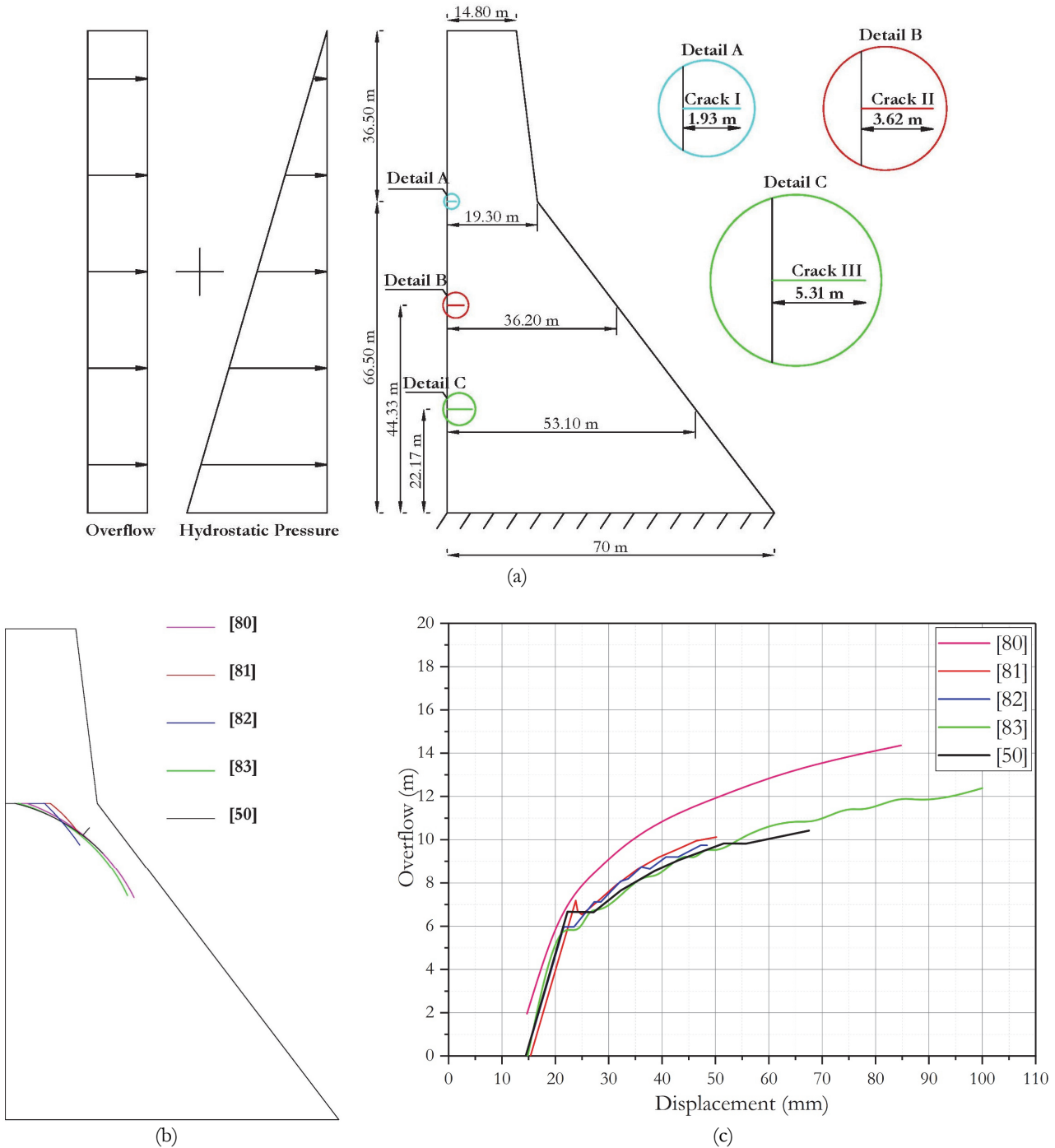


Figure 4: (a) Geometry of the Koyna dam. (b) Crack paths reported in previous works. c) Overflow against crest displacement reported in previous works.

The results of Case III are depicted in Fig. 7. The crest displacement is linear with the overflow up to the water level is 7.72 m above the crest of the dam (time step A). At that moment, the initial fracture suddenly propagates, and the crest displacements increase with a slight rise of the water level until the time step B. Afterward, the fracture propagates slowly, but the crest displacement increases with lower a lower rise of the water level. We stop the simulation when the overflow is 11 m.

The results of the last configuration, Case IV, are included in Fig. 8. This configuration includes the three initial fractures. Initially, the dam displacement is linear with the water level, until the level is 6.11 m above the crest at time step A. Between



the time steps A and B, the initial fracture located at the higher level –denoted crack I– experiences a sudden increase which makes the crest displacement also increase suddenly without apparent water level rise. Afterward, and between the time steps B and C, the previous fracture goes on propagating and makes the crest displacement no longer linear with the water level. Later, at time step C the initial fracture located at the lowest level –crack III– starts to propagate. The propagation continues until the fracture reaches the foundation at time step E. At this moment, the crack I branches, which makes the crest displacement increase suddenly until the time step F. Afterward, both branches of the fracture continue the propagation. But at time step G, the initial fracture at the middle level –crack II– begins to propagate. The simulation is stopped when the overflow is 11 m.

The crest displacement at the end of the simulation is almost 90 mm. This configuration, Case IV, provided higher crest displacements than the other three due to the presence of three initial fractures. The three initial fractures propagate at different time steps. The initial crack I --the one located at the highest level-- is the first fracture to grow and the propagation starts for the same overflow as for Case I, i.e., the configuration with only crack I.

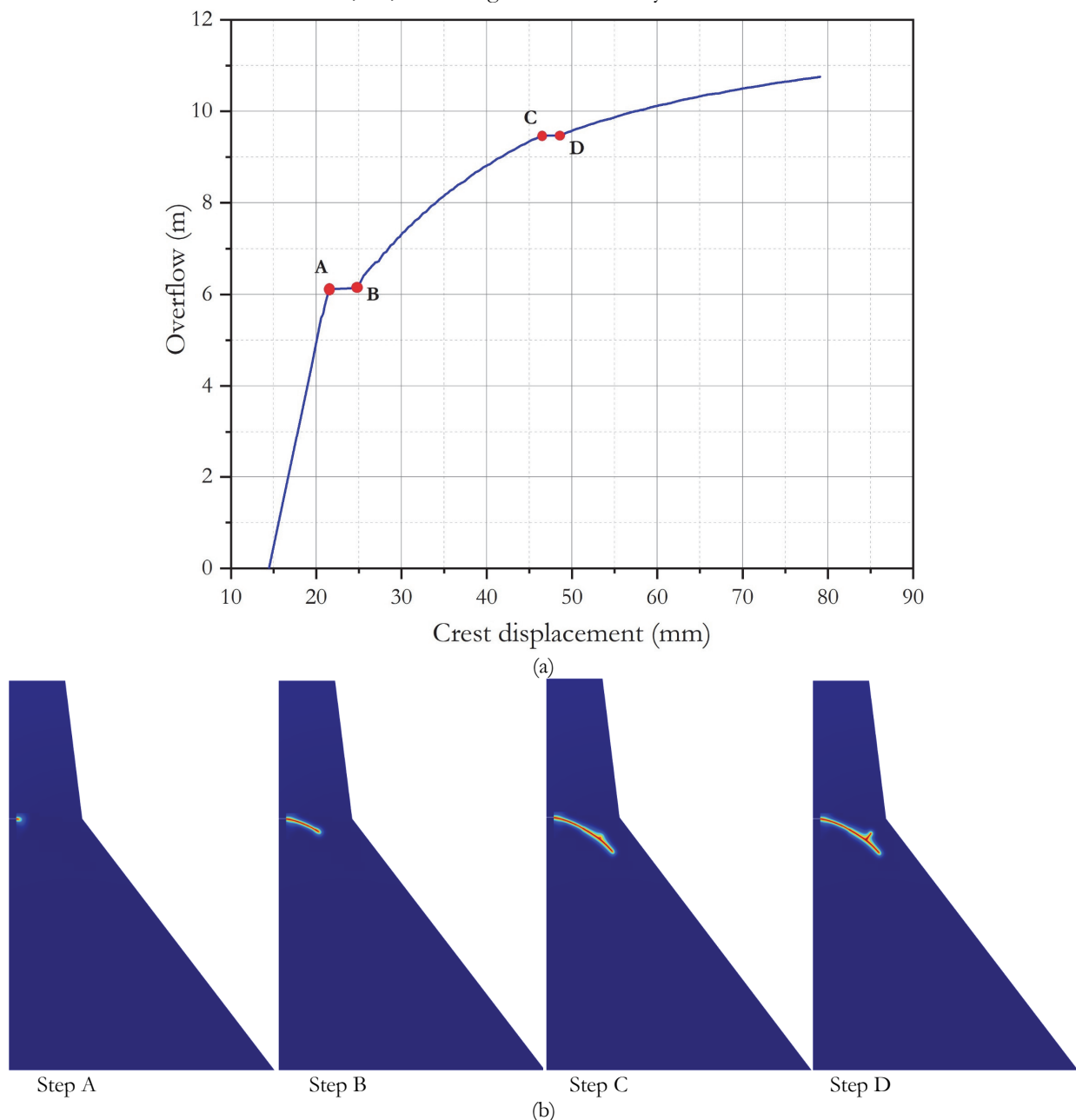


Figure 5: (a) Overflow against crest displacement for Case I with $G_c=100$ N/m. (b) Contour plots of the phase-field at four-time steps.

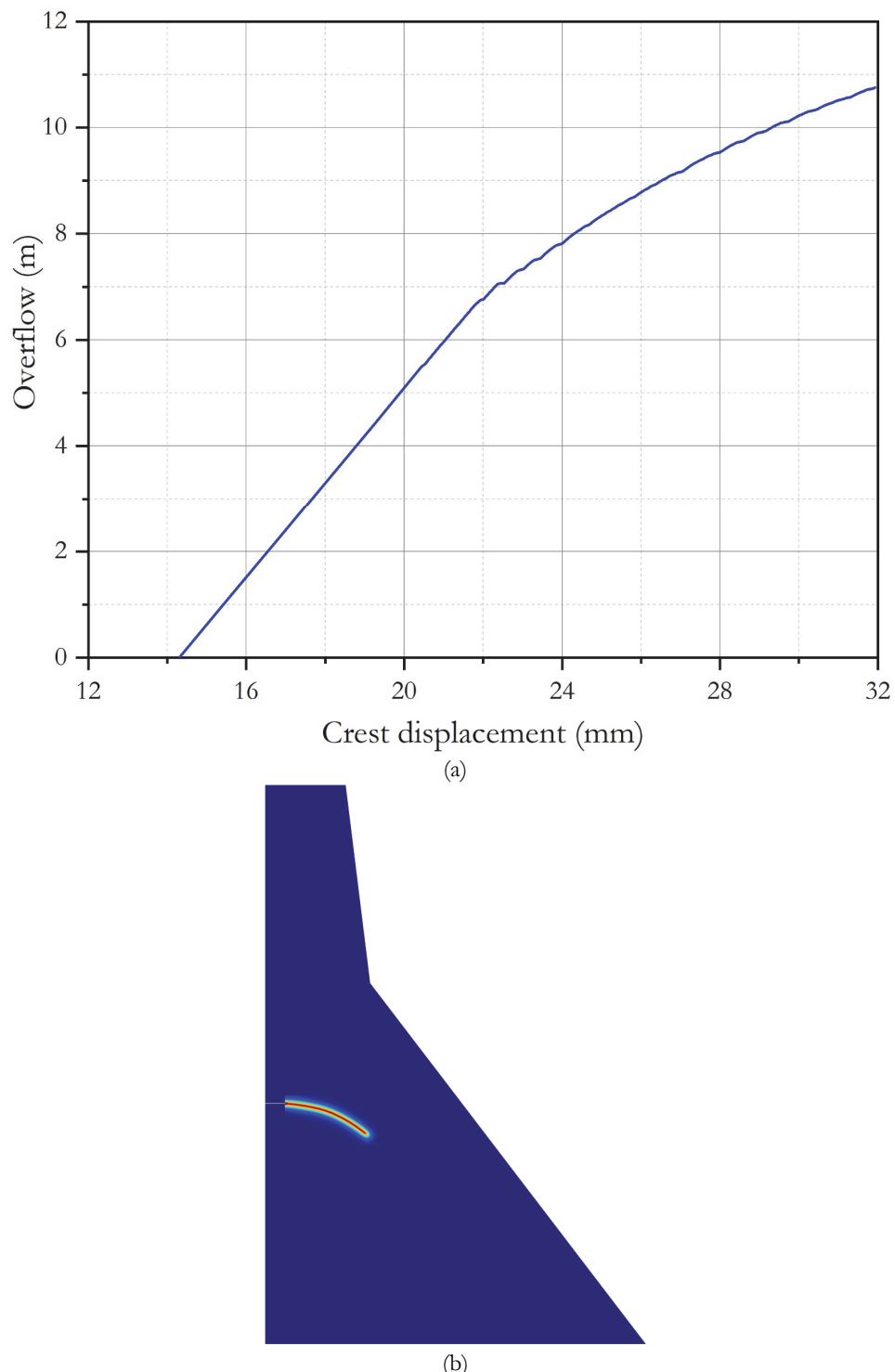


Figure 6: (a) Overflow against crest displacement for Case II with $G_c=100 \text{ N/m}$. (b) Contour plots of the phase-field at the end of the simulation.

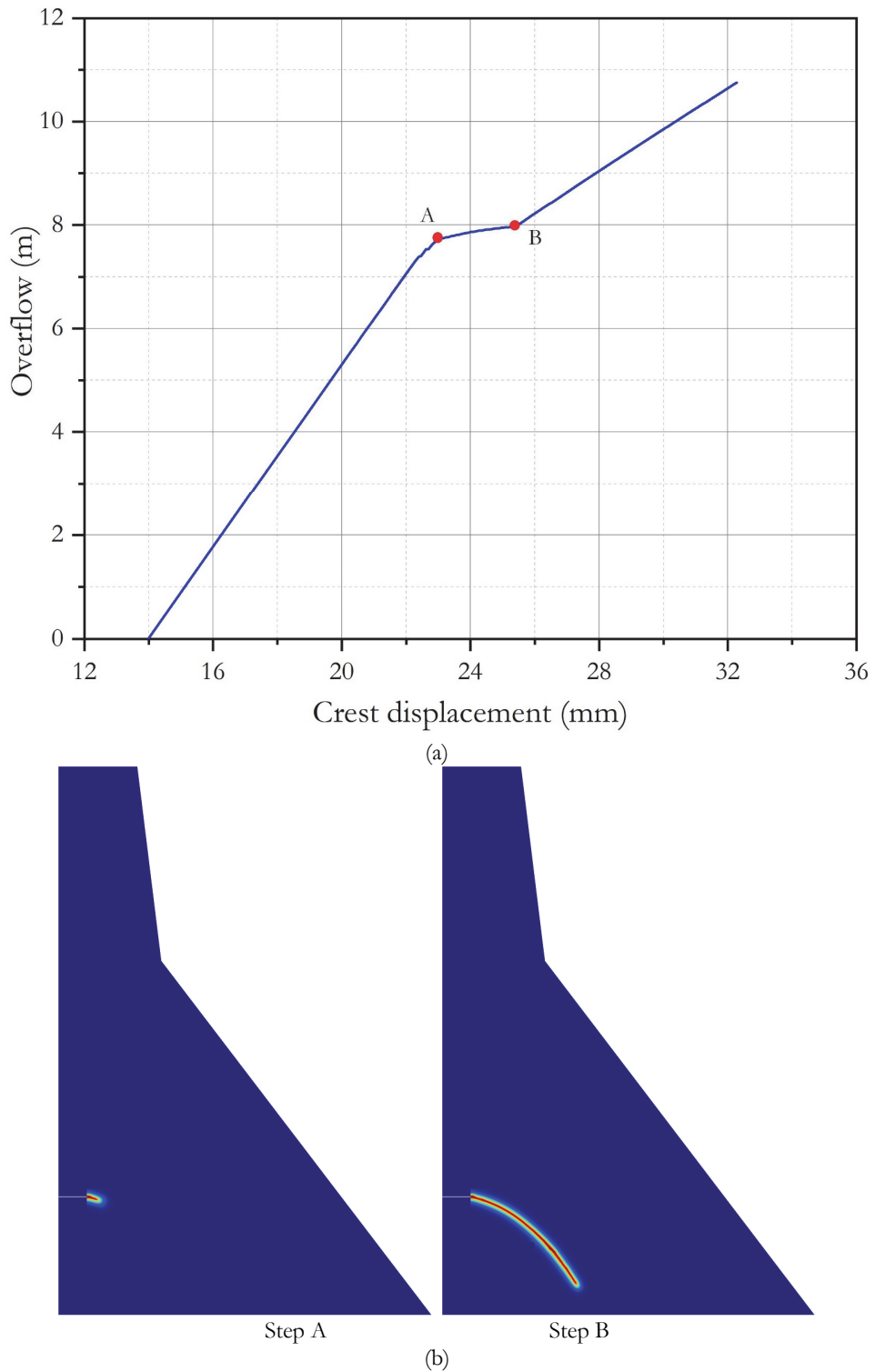
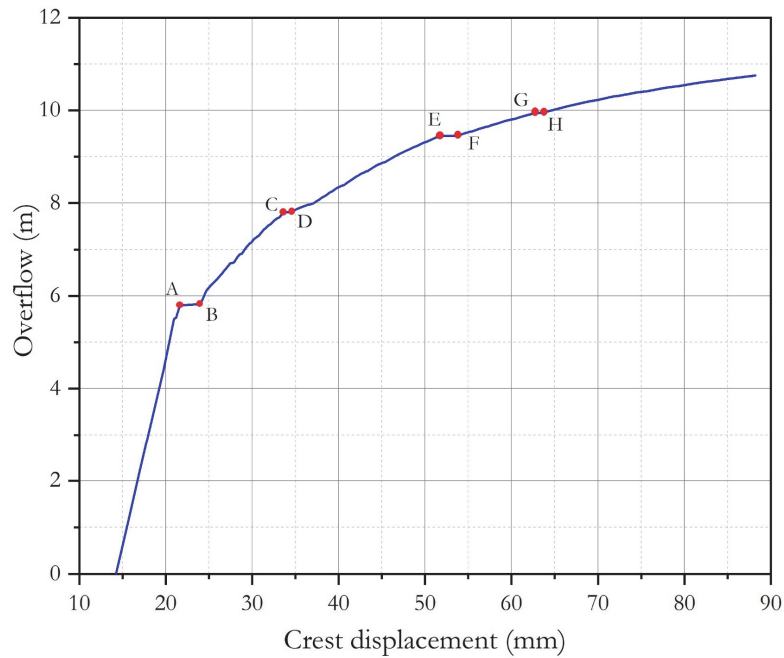


Figure 7: (a) Overflow against crest displacement for Case III with $G_c=100 \text{ N/m}$. (b) Contour plots of the phase-field at two-time steps.



(a)

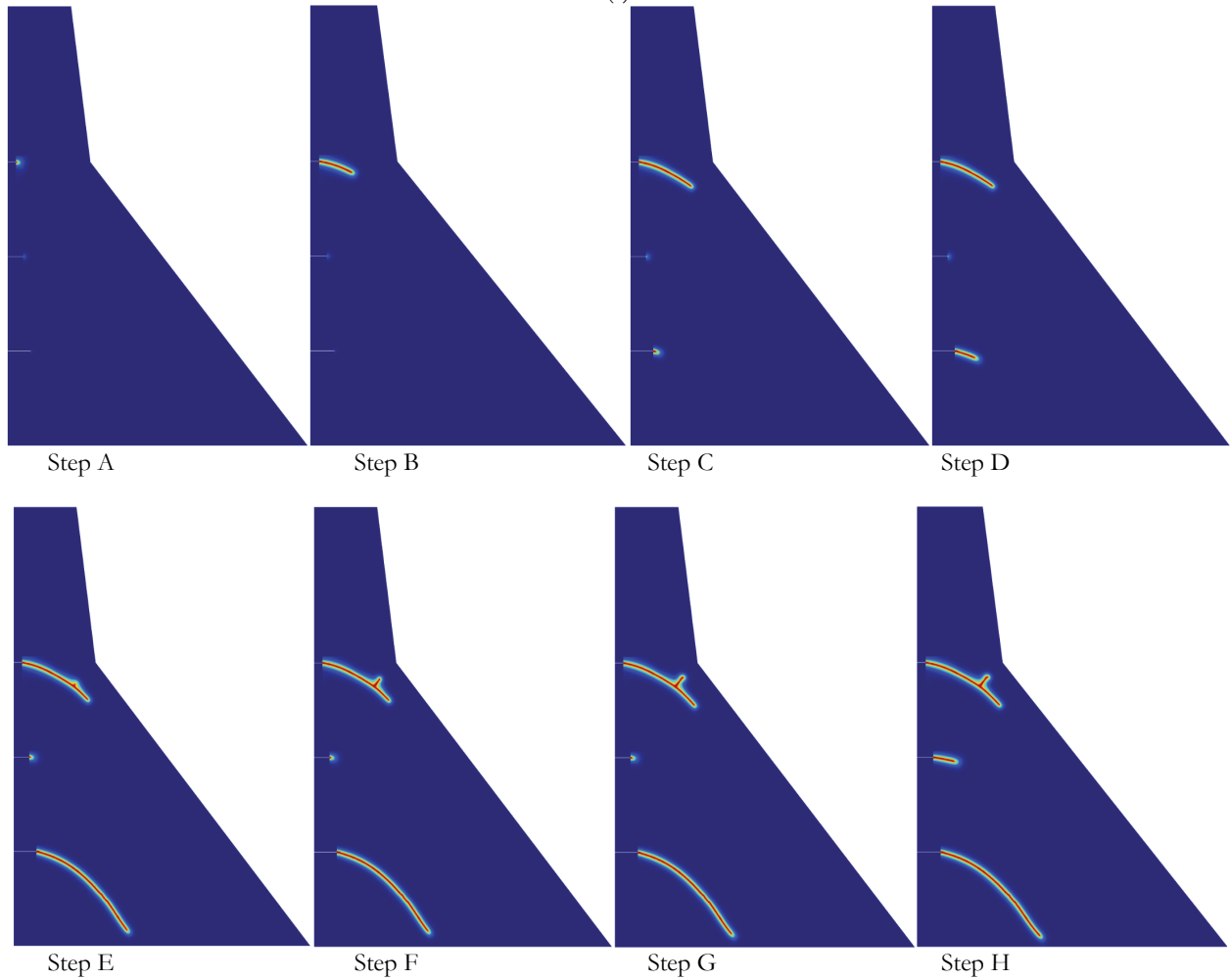


Figure 8: (a) Overflow against crest displacement for Case IV with $G_c=100 \text{ N/m}$. (b) Contour plots of the phase-field at eight-time steps.



Simulation for a rate $G_c=200 \text{ N/m}$

We describe and analyze the results of the simulation of our four adopted cases in this section with Griffith's critical energy release rate is now $G_c = 200 \text{ N/m}$. The result for the model with crack I –the initial fracture at the highest level, Case I– are included in Fig. 9. Both simulations with $G_c = 100 \text{ N/m}$ and $G_c = 200 \text{ N/m}$ present the same pattern of crest displacement evolution. Both simulations present two plateaus, the first one due to a sudden propagation of the initial fracture, and the second due to the branching of the fracture. However, the model with the highest toughness requires a higher overflow to initiate the fracture propagation. Nevertheless, for the same final overflow, 11 m, the final crest displacement is 80 mm in both simulations, i.e., the final crest displacement is almost independent of the toughness of concrete, as well as the final fracture pattern.

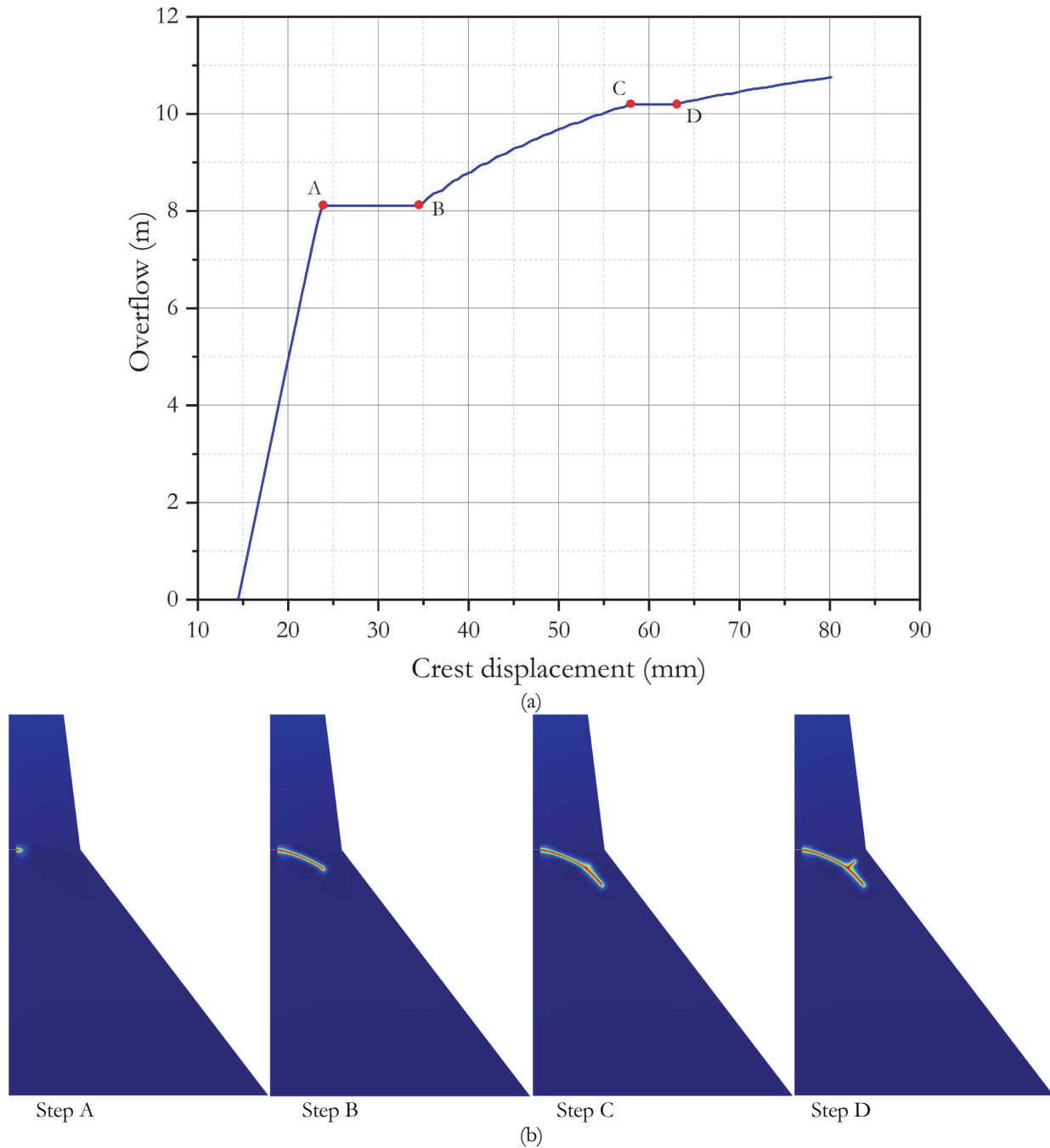


Figure 9: (a) Overflow against crest displacement for Case I with $G_c=200 \text{ N/m}$. (b) Contour plots of the phase-field at four-time steps.

The evolution of the crest displacement and final fracture pattern of Case II with toughness $G_c = 200 \text{ N/m}$, Fig. 10, differs from the case with toughness $G_c = 100 \text{ N/m}$. The case with the highest toughness requires a higher overflow to initiate the propagation of the fracture. Once the crack starts to grow, a sudden but short propagation occurs which makes the crest displace without almost water rise. Afterward, the crest goes on increasing with the rise in water level, although the fracture almost does not grow. The final overflow is 11 m, which produces a final crest displacement of 30.5 mm, slightly lower than the model with toughness $G_c = 100 \text{ N/m}$ where it is 32 mm. The plateau in the overflow-crest displacement curve is not given in the model with toughness $G_c = 100 \text{ N/m}$, as well as the final fracture is much longer.

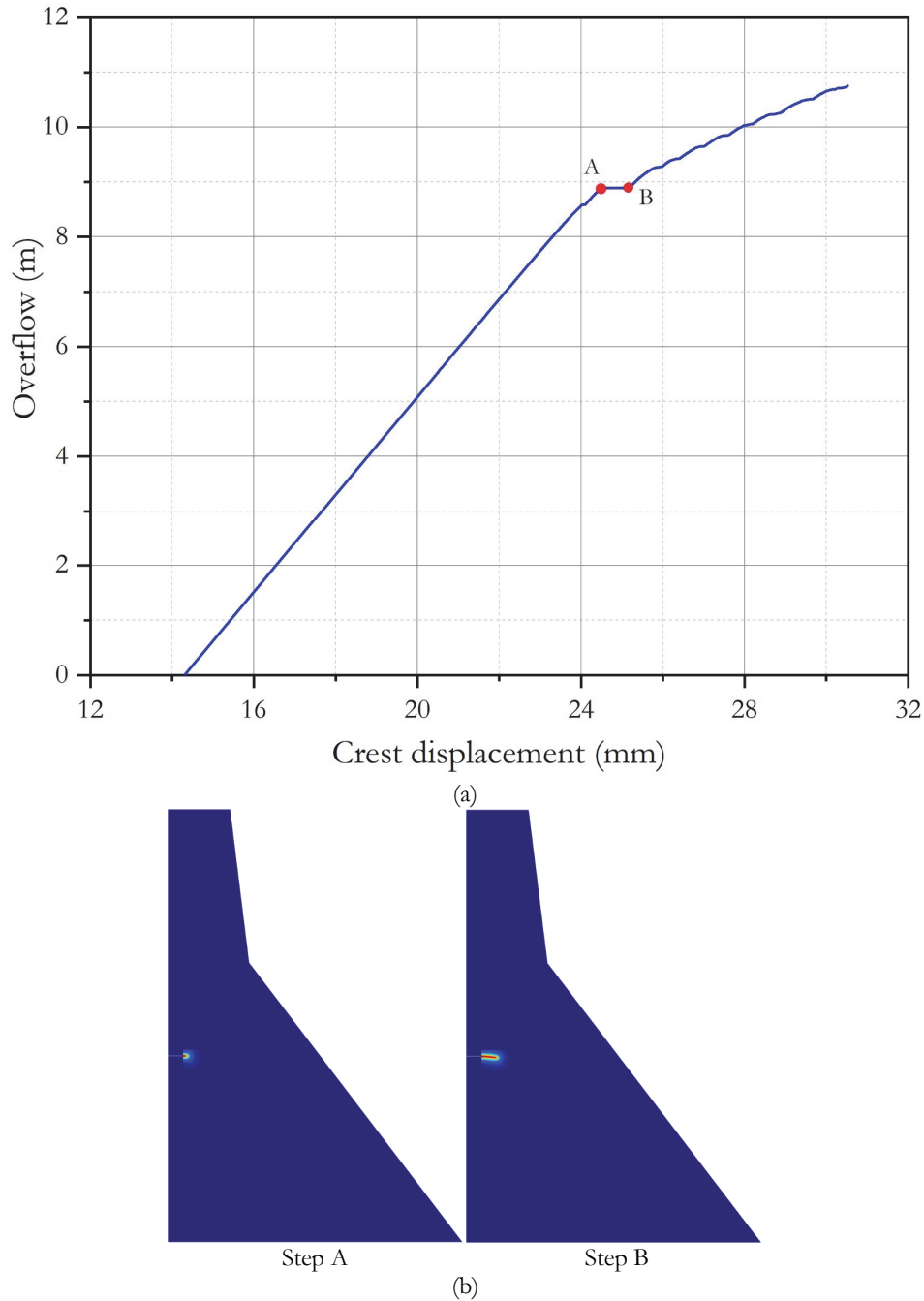


Figure 10: (a) Overflow against crest displacement for Case II with $G_c=200 \text{ N/m}$. (b) Contour plots of the phase-field at two-time steps.

Case III –initial fracture at the lowest level– with toughness $G_c = 200 \text{ N/m}$, Fig. 11, has a similar pattern to the case with toughness $G_c = 100 \text{ N/m}$. The fracture begins to propagate for a higher overflow in the case with $G_c=200 \text{ N/m}$, and



although both simulations have a plateau in the overflow-crest displacement, it becomes more pronounced for the case with the highest toughness. The final fracture pattern, as well as crest displacement, are almost identical for both cases, and consequently, independent of the concrete toughness.

Case IV with $G_c = 200 \text{ N/m}$, Fig. 12, includes the three initial fractures. The evolution of the crest displacement is quite similar to the case with $G_c = 100 \text{ N/m}$, although two main differences arise: one of the plateaus are not present in this case, and the first fracture begins to propagate for a higher overflow. The plateau is not presented because the initial fracture at the middle level, crack II, does not propagate, as shown in panel (b). The final patterns of the fractures are quite similar to the model with $G_c = 100 \text{ N/m}$, except for the absence of crack II. The value of the final crest displacement is also equal to the model with $G_c = 100 \text{ N/m}$.

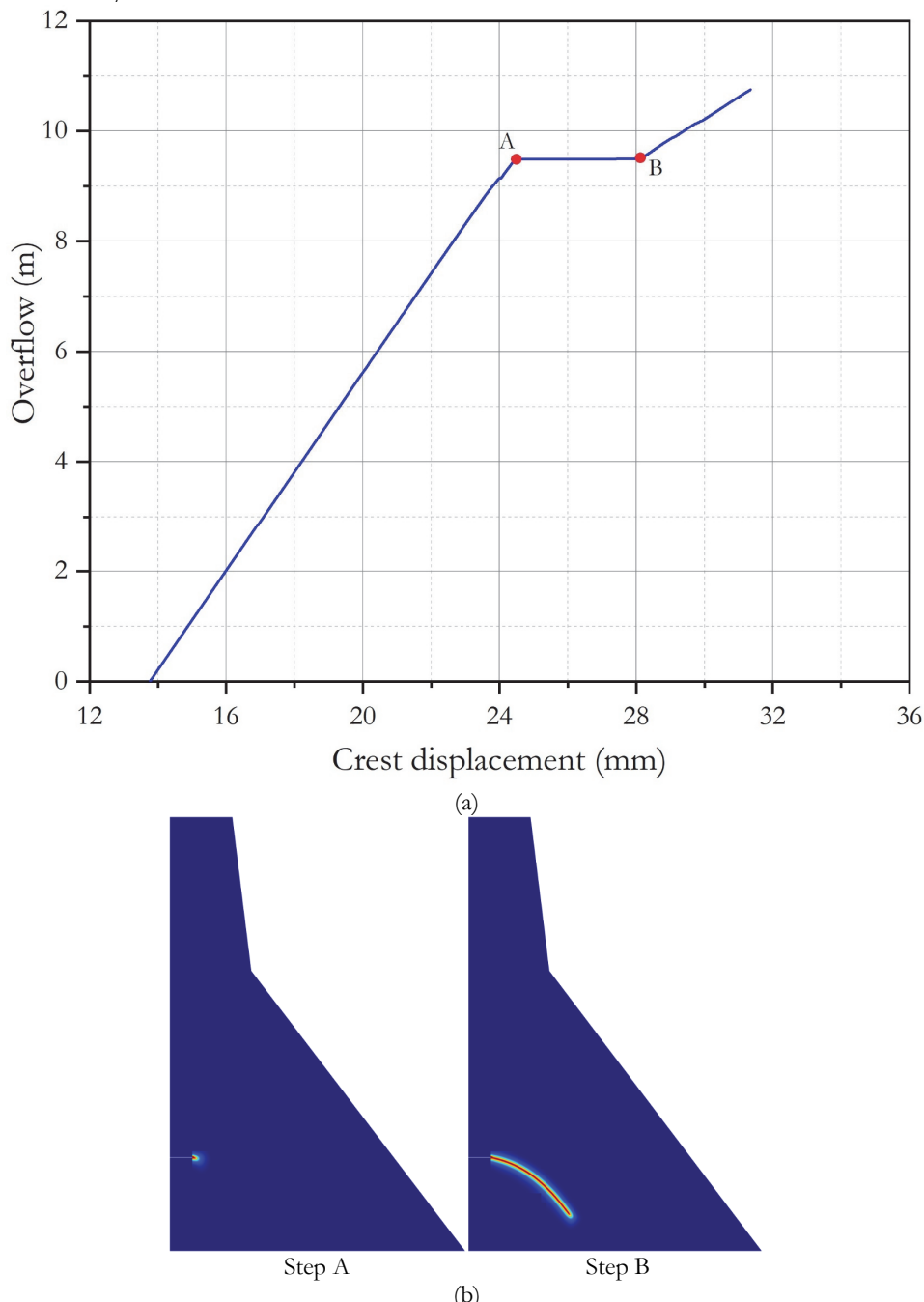


Figure 11: (a) Overflow against crest displacement for Case III with $G_c = 200 \text{ N/m}$. (b) Contour plots of the phase-field at two-time steps.

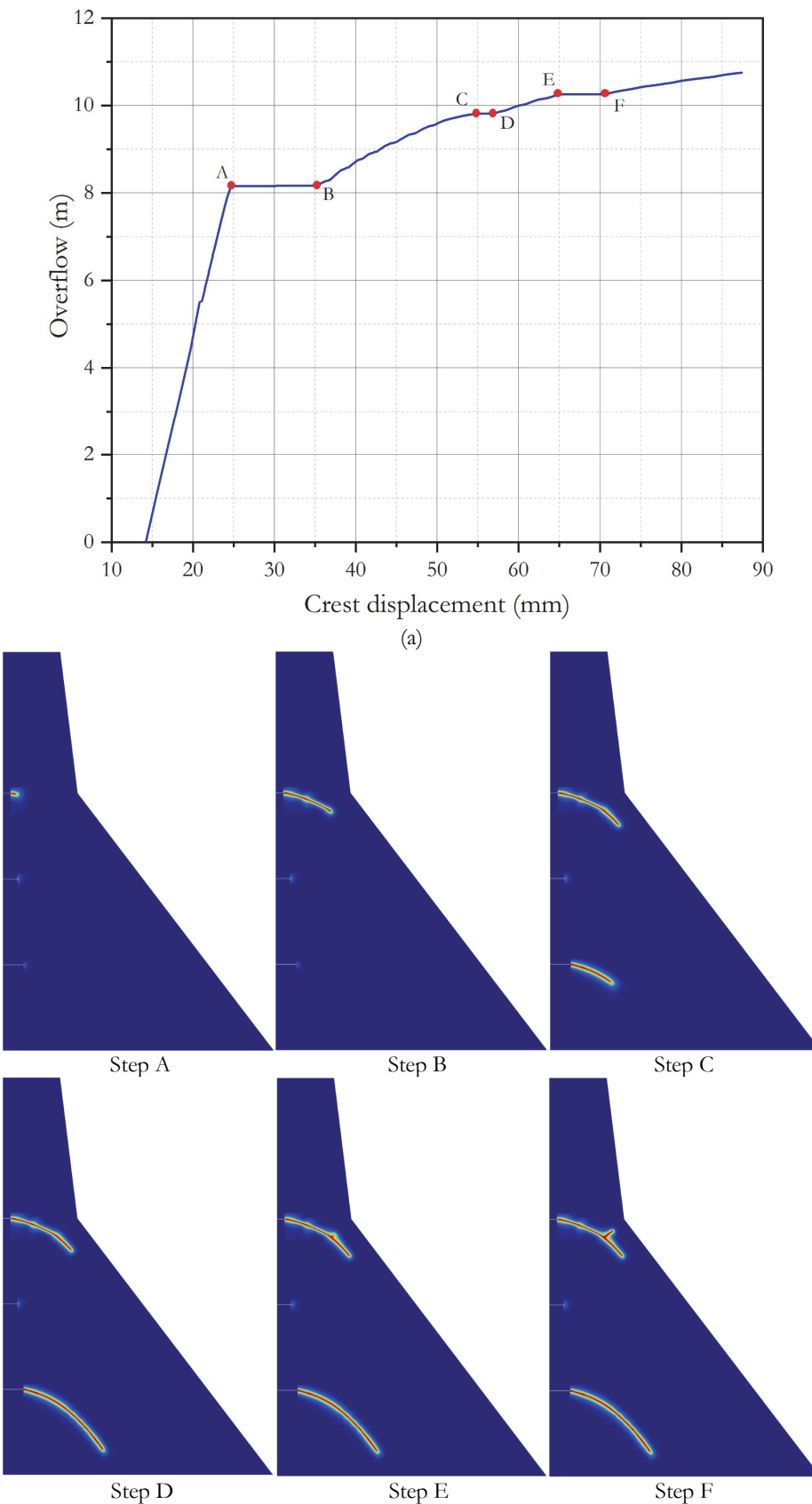


Figure 12: (a) Overflow against crest displacement for Case IV with $G_c = 200 \text{ N/m}$. (b) Contour plots of the phase-field at six-time steps.



CONCLUSIONS

In this work, we present a hybrid phase-field model to simulate the propagation of fractures under mode-I in brittle materials. We studied the behavior of a life-size structure, a concrete gravity dam, taking into account multi basic parameters that can considerably influence the structure stability.

We validated our model with a benchmark: the propagation of a fracture in a notched beam. Experimental and numerical results are available in the literature. Our numerical simulations provided similar results to those reported in the literature. In this line, our evolution of the applied load against the crack mouth opening displacement (CMOD) is quite similar to the results of other authors.

We applied our model to the study of a life-size structure, the Koyna dam. The structure is a 103 m height gravity dam located in India. It has been widely used as a benchmark model for static analysis of fracture propagation with 2-dimensional mathematical models. We analyzed four cases, three of them with only one initial small fracture in the upstream face at three levels, and the fourth case includes the three previous initial fractures, and we considered two values for the toughness of the concrete: Griffith critical energy release, G_c , equal to 100 N/m and 200 N/m. We simulated the propagation of the fractures under a flood episode.

The most adverse level of the initial fracture is the highest one. This case provided the highest crest displacements at the end of the simulation when the overflow was 11 m. This case was the most unfavorable because of fracture propagates along the thinnest part of the dam. The simulations with the two considered values of the Griffith energy release rate provided the same fracture patterns for the same initial fracture configurations. The overflow required to initiate the fracture propagation increased as G_c does. Nevertheless, once the fracture started to grow, the crest displacement for the final overflow, 11 m in all the simulations, was independent of the G_c -value. Consequently, concrete with enhanced toughness requires higher values of the overflow, but once fracture starts to propagate, the final fracture length and crest displacement are almost independent of concrete toughness.

Our simulations showed that phase-field models are suitable for life-size problems in civil engineering. They can be useful for design engineers as well as stakeholders and infrastructure operators in their safety assessment tasks. Our recommended phase-field approach turns out to be very convenient from the point of view of computations and ease of implementation for quasi-brittle structures.

REFERENCES

- [1] Griffits, A.A. (1921). VI. The phenomena of rupture and flow in solids, *Philos. Trans. R. Soc. London. Ser. A, Contain. Pap. a Math. or Phys. Character*, 221(582–593), pp. 163–198, DOI: 10.1098/rsta.1921.0006.
- [2] Bažant, Z.P. (1998). *Fracture and size effect in concrete and other quasibrittle materials*, CRC Press.
- [3] Rashid, Y.R. (1968). Ultimate strength analysis of prestressed concrete pressure vessels, *Nucl. Eng. Des.*, 7(4), pp. 334–344, DOI: 10.1016/0029-5493(68)90066-6.
- [4] Cundall, P.A., Strack, O.D.L. (1979). A discrete numerical model for granular assemblies, *Geotechnique*, 29(1), pp. 47–65, DOI: 10.1680/geot.1979.29.1.47.
- [5] Irwin, G.R. (1958). Fracture. *Symposia of the Society for Experimental Biology*, 34, pp. 551–590.
- [6] Barenblatt, G.I. (1959). The formation of equilibrium cracks during brittle fracture. General ideas and hypotheses. Axially-symmetric cracks, *J. Appl. Math. Mech.*, 23(3), pp. 622–636, DOI: 10.1016/0021-8928(59)90157-1.
- [7] Bažant, Z.P., Kim, J.K., Pfeiffer, P.A. (1986). Nonlinear fracture properties from size effect tests, *J. Struct. Eng. (United States)*, 112(2), pp. 289–307, DOI: 10.1061/(ASCE)0733-9445(1986)112:2(289).
- [8] Dugdale, D.S. (1960). Yielding of steel sheets containing slits, *J. Mech. Phys. Solids*, 8(2), pp. 100–104, DOI: 10.1016/0022-5096(60)90013-2.
- [9] Hillerborg, A., Modéer, M., Petersson, P.E. (1976). Analysis of crack formation and crack growth in concrete by means of fracture mechanics and finite elements, *Cem. Concr. Res.*, 6(6), pp. 773–781, DOI: 10.1016/0008-8846(76)90007-7.
- [10] Mindess, S. (1991). *The Fracture Process Zone in Concrete. Toughening Mechanisms in Quasi-Brittle Materials*, Dordrecht, Springer Netherlands, pp. 271–86.
- [11] Richard, H.A., Sander, M. (2016). Fundamentals of fracture mechanics, *Solid Mech. Its Appl.*, pp. 55–112, DOI: 10.1007/978-3-319-32534-7_3.
- [12] Kachanov, L.M. (1986). *Introduction to continuum damage mechanics*, vol. 10, Dordrecht, Springer Netherlands.
- [13] Lemaitre, J., Chaboche, J.-L. (1990). *Mechanics of Solid Materials*, Cambridge, Cambridge University Press.



- [14] Krajcinovic, D. (1989). Damage mechanics, *Mech. Mater.*, 8(2–3), pp. 117–197, DOI: 10.1016/0167-6636(89)90011-2.
- [15] Murakami, S. (2012). *Continuum Damage Mechanics: A Continuum Mechanics Approach to the Analysis of Damage and Fracture*, 185, Dordrecht, Springer Netherlands.
- [16] Mazars, J. (1984). Application de la mécanique de l'endommagement au comportement non linéaire et à la rupture du béton de structure. Université Pierre et Marie Curie.
- [17] Ortiz, M. (1985). A constitutive theory for the inelastic behavior of concrete, *Mech. Mater.*, 4(1), pp. 67–93, DOI: 10.1016/0167-6636(85)90007-9.
- [18] Resende, L. (1987). A Damage mechanics constitutive theory for the inelastic behaviour of concrete, *Comput. Methods Appl. Mech. Eng.*, 60(1), pp. 57–93, DOI: 10.1016/0045-7825(87)90130-7.
- [19] Yazdani, S., Schreyer, H.L. (1990). Combined Plasticity and Damage Mechanics Model for Plain Concrete, *J. Eng. Mech.*, 116(7), pp. 1435–1450, DOI: 10.1061/(ASCE)0733-9399(1990)116:7(1435).
- [20] Oller, S., Oñate, E., Oliver, J., Lubliner, J. (1990). Finite element nonlinear analysis of concrete structures using a “plastic-damage model,” *Eng. Fract. Mech.*, 35(1–3), pp. 219–231, DOI: 10.1016/0013-7944(90)90200-Z.
- [21] Mazars, J., Berthaud, Y., Ramtani, S. (1990). The unilateral behaviour of damaged concrete, *Eng. Fract. Mech.*, 35(4–5), pp. 629–635, DOI: 10.1016/0013-7944(90)90145-7.
- [22] Halm, D., Dragon, A. (1998). An anisotropic model of damage and frictional sliding for brittle materials, *Eur. J. Mech. - A/Solids*, 17(3), pp. 439–460, DOI: 10.1016/S0997-7538(98)80054-5.
- [23] Fichant, S., La Borderie, C., Pijaudier-Cabot, G. (1999). Isotropic and anisotropic descriptions of damage in concrete structures, *Mech. Cohesive-Frictional Mater.*, 4(4), pp. 339–359, DOI: 10.1002/(SICI)1099-1484(199907)4:4<339::AID-CFM65>3.0.CO;2-J.
- [24] Ragueneau, F., La Borderie, C., Mazars, J. (2000). Damage model for concrete-like materials coupling cracking and friction, contribution towards structural damping: first uniaxial applications, *Mech. Cohesive-Frictional Mater.*, 5(8), pp. 607–625, DOI: 10.1002/1099-1484(200011)5:8<607::AID-CFM108>3.0.CO;2-K.
- [25] Geers, M.G.D., de Borst, R., Peerlings, R.H.J. (2000). Damage and crack modeling in single-edge and double-edge notched concrete beams, *Eng. Fract. Mech.*, 65(2–3), pp. 247–61, DOI: 10.1016/S0013-7944(99)00118-6.
- [26] Chan, S.K., Tuba, I.S., Wilson, W.K. (1970). On the finite element method in linear fracture mechanics, *Eng. Fract. Mech.*, 2(1), pp. 1–17, DOI: 10.1016/0013-7944(70)90026-3.
- [27] Sih, G.C. (1974). Strain-energy-density factor applied to mixed mode crack problems, *Int. J. Fract.*, 10(3), pp. 305–321, DOI: 10.1007/BF00035493.
- [28] Bittencourt, T.N., Wawrynek, P.A., Ingraffea, A.R., Sousa, J.L. (1996). Quasi-automatic simulation of crack propagation for 2D LEFM problems, *Eng. Fract. Mech.*, 55(2), pp. 321–334, DOI: 10.1016/0013-7944(95)00247-2.
- [29] Pavlou, D., Labeas, G., Vlachakis, N., Pavlou, F. (2003). Fatigue crack propagation trajectories under mixed-mode cyclic loading, *Eng. Struct.*, 25(7), pp. 869–875, DOI: 10.1016/S0141-0296(03)00018-X.
- [30] Alshoaiib, A.M., Ariffin, A.K. (2006). Finite element simulation of stress intensity factors in elastic-plastic crack growth, *J. Zhejiang Univ. A*, 7(8), pp. 1336–1342, DOI: 10.1631/jzus.2006.A1336.
- [31] Aour, B., Rahmani, O., Nait-Abdelaziz, M. (2007). A coupled FEM/BEM approach and its accuracy for solving crack problems in fracture mechanics, *Int. J. Solids Struct.*, 44(7–8), pp. 2523–2539, DOI: 10.1016/j.ijsolstr.2006.08.001.
- [32] Souiyah, M., Alshoaiib, A., Muchtar, A., Ariffin, A.K. (2008). Finite element model for linear-elastic mixed mode loading using adaptive mesh strategy, *J. Zhejiang Univ. A*, 9(1), pp. 32–37, DOI: 10.1631/jzus.A072176.
- [33] Khoei, A.R., Moslemi, H., Majd Ardakany, K., Barani, O.R., Azadi, H. (2009). Modeling of cohesive crack growth using an adaptive mesh refinement via the modified-SPR technique, *Int. J. Fract.*, 159(1), pp. 21–41, DOI: 10.1007/s10704-009-9380-1.
- [34] Dong, W., Wu, Z., Tang, X., Zhou, X. (2018). A comparative study on stress intensity factor-based criteria for the prediction of mixed mode I-II crack propagation in concrete, *Eng. Fract. Mech.*, 197, pp. 217–235, DOI: 10.1016/j.engfracmech.2018.05.009.
- [35] Sukumar, N., Huang, Z.Y., Prévost, J.-H., Suo, Z. (2004). Partition of unity enrichment for bimaterial interface cracks, *Int. J. Numer. Methods Eng.*, 59(8), pp. 1075–1102, DOI: 10.1002/nme.902.
- [36] Liu, X.Y., Xiao, Q.Z., Karighaloo, B.L. (2004). XFEM for direct evaluation of mixed mode SIFs in homogeneous and bi-materials, *Int. J. Numer. Methods Eng.*, 59(8), pp. 1103–18, DOI: 10.1002/nme.906.
- [37] Elguedj, T., Gravouil, A., Combescure, A. (2006). Appropriate extended functions for X-FEM simulation of plastic fracture mechanics, *Comput. Methods Appl. Mech. Eng.*, 195(7–8), pp. 501–515, DOI: 10.1016/j.cma.2005.02.007.
- [38] Asadpoure, A., Mohammadi, S. (2007). Developing new enrichment functions for crack simulation in orthotropic media by the extended finite element method, *Int. J. Numer. Methods Eng.*, 69(10), pp. 2150–2172, DOI: 10.1002/nme.1839.
- [39] Duddu, R., Bordas, S., Chopp, D., Moran, B. (2008). A combined extended finite element and level set method for



- biofilm growth, *Int. J. Numer. Methods Eng.*, 74(5), pp. 848–870, DOI: 10.1002/nme.2200.
- [40] Khoei, A.R., Karimi, K. (2008). An enriched-FEM model for simulation of localization phenomenon in Cosserat continuum theory, *Comput. Mater. Sci.*, 44(2), pp. 733–749, DOI: 10.1016/j.commatsci.2008.05.019.
- [41] Cox, J. V. (2009). An extended finite element method with analytical enrichment for cohesive crack modeling, *Int. J. Numer. Methods Eng.*, 78(1), pp. 48–83, DOI: 10.1002/nme.2475.
- [42] Menouillard, T., Belytschko, T. (2009). Correction force for releasing crack tip element with XFEM and only discontinuous enrichment, *Eur. J. Comput. Mech.*, 18(5–6), pp. 465–483, DOI: 10.3166/ejcm.18.465-483.
- [43] Yu, T.T., Liu, P. (2011). Improved implementation of the extended finite element method for stress analysis around cracks, *Arch. Civ. Mech. Eng.*, 11(3), pp. 787–805, DOI: 10.1016/s1644-9665(12)60116-2.
- [44] Francfort, G.A., Marigo, J.-J. (1998). Revisiting brittle fracture as an energy minimization problem, *J. Mech. Phys. Solids*, 46(8), pp. 1319–1342, DOI: 10.1016/S0022-5096(98)00034-9.
- [45] Bourdin, B., Francfort, G.A., Marigo, J.-J. (2000). Numerical experiments in revisited brittle fracture, *J. Mech. Phys. Solids*, 48(4), pp. 797–826, DOI: 10.1016/S0022-5096(99)00028-9.
- [46] Aranson, I.S., Kalatsky, V.A., Vinokur, V.M. (2000). Continuum field description of crack propagation, *Phys. Rev. Lett.*, 85(1), pp. 118–121, DOI: 10.1103/PhysRevLett.85.118.
- [47] Bourdin, B., Francfort, G.A., Marigo, J.-J. (2008). The variational approach to fracture, Dordrecht, Springer Netherlands.
- [48] Miehe, C., Hofacker, M., Welschinger, F. (2010). A phase field model for rate-independent crack propagation: Robust algorithmic implementation based on operator splits, *Comput. Methods Appl. Mech. Eng.*, 199(45–48), pp. 2765–2778, DOI: 10.1016/j.cma.2010.04.011.
- [49] Wu, J.-Y. (2017). A unified phase-field theory for the mechanics of damage and quasi-brittle failure, *J. Mech. Phys. Solids*, 103, pp. 72–99, DOI: 10.1016/j.jmps.2017.03.015.
- [50] Santillán, D., Mosquera, J.C., Cueto-Felgueroso, L. (2017). Phase-field model for brittle fracture. Validation with experimental results and extension to dam engineering problems, *Eng. Fract. Mech.*, 178, pp. 109–125, DOI: 10.1016/j.engfracmech.2017.04.020.
- [51] Amor, H., Marigo, J.-J., Maurini, C. (2009). Regularized formulation of the variational brittle fracture with unilateral contact: Numerical experiments, *J. Mech. Phys. Solids*, 57(8), pp. 1209–1229, DOI: 10.1016/j.jmps.2009.04.011.
- [52] Nguyen, T.T., Yvonnet, J., Bornert, M., Chateau, C., Sab, K., Romani, R., Le Roy, R. (2016). On the choice of parameters in the phase field method for simulating crack initiation with experimental validation, *Int. J. Fract.*, 197(2), pp. 213–226, DOI: 10.1007/s10704-016-0082-1.
- [53] Santillán, D., Mosquera, J.-C., Cueto-Felgueroso, L. (2017). Fluid-driven fracture propagation in heterogeneous media: Probability distributions of fracture trajectories, *Phys. Rev. E*, 96(5), pp. 053002, DOI: 10.1103/PhysRevE.96.053002.
- [54] Santillán, D., Juanes, R., Cueto-Felgueroso, L. (2018). Phase Field Model of Hydraulic Fracturing in Poroelastic Media: Fracture Propagation, Arrest, and Branching Under Fluid Injection and Extraction, *J. Geophys. Res. Solid Earth*, 123(3), pp. 2127–2155, DOI: 10.1002/2017JB014740.
- [55] Lancioni, G., Royer-Carfagni, G. (2009). The Variational Approach to Fracture Mechanics. A Practical Application to the French Panthéon in Paris, *J. Elast.*, 95(1–2), pp. 1–30, DOI: 10.1007/s10659-009-9189-1.
- [56] Borden, M.J., Hughes, T.J.R., Landis, C.M., Verhoosel, C. V. (2014). A higher-order phase-field model for brittle fracture: Formulation and analysis within the isogeometric analysis framework, *Comput. Methods Appl. Mech. Eng.*, 273, pp. 100–118, DOI: 10.1016/j.cma.2014.01.016.
- [57] Santillán, D., Juanes, R., Cueto-Felgueroso, L. (2017). Phase field model of fluid-driven fracture in elastic media: Immersed-fracture formulation and validation with analytical solutions, *J. Geophys. Res. Solid Earth*, 122(4), pp. 2565–2589, DOI: 10.1002/2016JB013572.
- [58] Alessi, R., Marigo, J.-J., Vidoli, S. (2015). Gradient damage models coupled with plasticity: Variational formulation and main properties, *Mech. Mater.*, 80, pp. 351–367, DOI: 10.1016/j.mechmat.2013.12.005.
- [59] Ambati, M., Gerasimov, T., De Lorenzis, L. (2015). Phase-field modeling of ductile fracture, *Comput. Mech.*, 55(5), pp. 1017–1040, DOI: 10.1007/s00466-015-1151-4.
- [60] Borden, M.J., Hughes, T.J.R., Landis, C.M., Anvari, A., Lee, I.J. (2016). A phase-field formulation for fracture in ductile materials: Finite deformation balance law derivation, plastic degradation, and stress triaxiality effects, *Comput. Methods Appl. Mech. Eng.*, 312, pp. 130–166, DOI: 10.1016/j.cma.2016.09.005.
- [61] Kuhn, C., Noll, T., Müller, R. (2016). On phase field modeling of ductile fracture, *GAMM-Mitteilungen*, 39(1), pp. 35–54, DOI: 10.1002/gamm.201610003.
- [62] Verhoosel, C. V., de Borst, R. (2013). A phase-field model for cohesive fracture, *Int. J. Numer. Methods Eng.*, 96(1), pp. 43–62, DOI: 10.1002/nme.4553.
- [63] Vignollet, J., May, S., de Borst, R., Verhoosel, C. V. (2014). Phase-field models for brittle and cohesive fracture,



- Meccanica, 49(11), pp. 2587–601, DOI: 10.1007/s11012-013-9862-0.
- [64] May, S., Vignollet, J., de Borst, R. (2015). A numerical assessment of phase-field models for brittle and cohesive fracture: Γ -Convergence and stress oscillations, *Eur. J. Mech. - A/Solids*, 52, pp. 72–84, DOI: 10.1016/j.euromechsol.2015.02.002.
- [65] Borden, M.J., Verhoosel, C. V., Scott, M.A., Hughes, T.J.R., Landis, C.M. (2012). A phase-field description of dynamic brittle fracture, *Comput. Methods Appl. Mech. Eng.*, 217–220, pp. 77–95, DOI: 10.1016/j.cma.2012.01.008.
- [66] Zhang, X., Vignes, C., Sloan, S.W., Sheng, D. (2017). Numerical evaluation of the phase-field model for brittle fracture with emphasis on the length scale, *Comput. Mech.*, 59(5), pp. 737–752, DOI: 10.1007/s00466-017-1373-8.
- [67] Irwin, G.R. (1970). Fracture strength of relatively brittle structures and materials, *J. Franklin Inst.*, 290(6), pp. 513–521, DOI: 10.1016/0016-0032(70)90234-6.
- [68] Miehe, C., Welschinger, F., Hofacker, M. (2010). Thermodynamically consistent phase-field models of fracture: Variational principles and multi-field FE implementations, *Int. J. Numer. Methods Eng.*, 83(10), pp. 1273–1311, DOI: 10.1002/nme.2861.
- [69] Lomiz, G.M. (1951). Flow in Fractured Rocks (Russian), Gosenergoizdat, Moscow, 127(197), pp. 635.
- [70] Louis, C. (1972). Rock Hydraulics. Rock Mechanics, Vienna, Springer Vienna, pp. 299–387.
- [71] White, F.M. (2016). Fluid Mechanics, McGraw-Hill Education.
- [72] Miehe, C., Hofacker, M., Welschinger, F. (2010). A phase field model for rate-independent crack propagation: Robust algorithmic implementation based on operator splits, *Comput. Methods Appl. Mech. Eng.*, 199(45–48), pp. 2765–2778, DOI: 10.1016/j.cma.2010.04.011.
- [73] Ambati, M., Gerasimov, T., De Lorenzis, L. (2014). A review on phase-field models of brittle fracture and a new fast hybrid formulation, *Comput. Mech.*, 55(2), pp. 383–405, DOI: 10.1007/s00466-014-1109-y.
- [74] Detournay, E. (2004). Propagation Regimes of Fluid-Driven Fractures in Impermeable Rocks, *Int. J. Geomech.*, 4(1), pp. 35–45, DOI: 10.1061/(ASCE)1532-3641(2004)4:1(35).
- [75] Ponce-Farfán, C., Santillán, D., Toledo, M.Á. (2020). Thermal Simulation of Rolled Concrete Dams: Influence of the Hydration Model and the Environmental Actions on the Thermal Field, *Water*, 12(3), pp. 858, DOI: 10.3390/w12030858.
- [76] Hindmarsh, A.C., Brown, P.N., Grant, K.E., Lee, S.L., Serban, R., Shumaker, D.E., Woodward, C.S. (2005). SUNDIALS: Suite of nonlinear and differential algebraic equation solvers, *ACM Trans. Math. Softw.*, 31(3), pp. 363–396, DOI: 10.1145/1089014.1089020.
- [77] Perdikaris, P.C., Romeo, A. (1995). Size effect on fracture energy of concrete and stability issues in three-point bending fracture toughness testing, *ACI Mater. J.*, 92(5), pp. 483–496.
- [78] Meschke, G., Lackner, R., Mang, H.A. (1998). An anisotropic elastoplastic-damage model for plain concrete, *Int. J. Numer. Methods Eng.*, 42(4), pp. 703–727, DOI: 10.1002/(SICI)1097-0207(19980630)42:4<703::AID-NME384>3.0.CO;2-B.
- [79] Mandal, T.K., Nguyen, V.P., Wu, J.Y. (2019). Length scale and mesh bias sensitivity of phase-field models for brittle and cohesive fracture, *Eng. Fract. Mech.*, 217(July), pp. 106532, DOI: 10.1016/j.engfracmech.2019.106532.
- [80] Gioia, G., Bažant, Z.P. (1992). Is no-tension dam design always safe? - A numerical study, *Dam Eng.*, 3(1), pp. 23–34.
- [81] Bhattacharjee, S.S., Léger, P. (1994). Application of NLFM models to predict cracking in concrete gravity dams, *J. Struct. Eng. (United States)*, 120(4), pp. 1255–1271, DOI: 10.1061/(ASCE)0733-9445(1994)120:4(1255).
- [82] Ghrib, F., Tinawi, R. (1995). Nonlinear behavior of concrete dams using damage mechanics, *J. Eng. Mech.*, 121(4), pp. 513–527, DOI: 10.1061/(ASCE)0733-9399(1995)121:4(513).
- [83] Roth, S.N., Léger, P., Soulaïmani, A. (2015). A combined XFEM-damage mechanics approach for concrete crack propagation, *Comput. Methods Appl. Mech. Eng.*, 283, pp. 923–955, DOI: 10.1016/j.cma.2014.10.043.
- [84] Bažant, Z.P., Planas, J. (2019). Fracture and Size Effect in Concrete and Other Quasibrittle Materials, 53, Routledge.